Transferability of the Deep Potential Model for Simulating Water-Graphene Confined System

Dongfei Liu^a, Jianzhong Wu^{b*}, Diannan Lu^{a*}

^a Department of Chemical Engineering, Tsinghua University, Beijing 100084, P. R. China

^b Department of Chemical and Environmental Engineering, University of California, Riverside,
California 92521, United States

To whom all correspondence should be addressed: jwu@engr.ucr.edu.cn; ludiannan@tsinghua.edu.cn

ABSTRACT: Machine learning potentials (MLPs) are poised to combine the accuracy of *ab initio* predictions with the computational efficiency of the classical molecular dynamics (MD) simulation. Whereas great progress has been made over the last two decades in developing MLPs, many challenges remain in their widespread applications due to the limitations of atom-based descriptors for representing long-range interactions and correlation effects. In this work, we evaluate two deep potential (DP) models for liquid water near graphene surfaces, Model S and Model F, with the latter having more training data. A concurrent learning algorithm (DP-GEN) is adopted to explore the configurational space beyond the scope of conventional *ab initio* MD simulation. The accuracy and reliability of the DP models have been examined in terms of their applicability to systems larger than those considered in the training dataset. We find that an

accurate prediction of atomic forces does not imply an accurate prediction of the system energy. The deviation from the relative atomic forces alone is insufficient to assess the transferability of the DP models. An alternative criterion is proposed by including both the energy and force deviations as measured by the root-mean-square error (RMSE) relative to the original test dataset. By evaluating the variation of potential energy with time and contrasting the relevant statistical features of diverse systems in both DPMD and classical MD simulations, we further elucidate the robust transferability of Model F, thus validating the above criterion.

Introduction

Interfacial water exhibits structural and dynamical properties distinctively different from those in the bulk phase. 1-21 Many computational studies have been carried out to study the properties of inhomogeneous water using classical molecular dynamics (MD) simulation. 3,4,7,12,16-21 The conventional models such as SPC/E and TIPnP/X can describe the bulk properties but their performance for nanoscale systems is often problematic due to the non-classical behavior of intermolecular interactions. 22 In principle, *ab initio* MD (AIMD) is applicable to liquid water at both bulk and inhomogeneous conditions. However, the computational cost of AIMD is prohibitive for large systems that entail long-time dynamic behavior. Over the past two decades, machine-learning potentials (MLPs) have been introduced to fill the gap between *ab initio* and classical MD simulations. 23-30 On the one hand, MLPs can capture the complex features of the potential energy surface (PES) obtained from accurate electronic structure calculations. On the other hand, the well-trained MLPs predict the potential energy and atomic force at a high level of accuracy with a computational cost negligible in comparison to the density functional theory (DFT) calculations.

Many MLPs are available from the literature, ranging from different forms of neural network potentials (NNPs)^{31–37} to kernel-based potentials such as gradient-domain machine learning (GDML)³⁸, Gaussian approximation potentials (GAPs)³⁹, spectral neighbor analysis potentials (SNAPs)⁴⁰, among other methods⁴¹. Existing MLPs are mostly based on atom-based descriptors and the locality approximation originally proposed by Behler and Parrinello²³. It is often assumed that atomic interactions can be described by the local chemical environments of individual atoms. The intermolecular potential is specified by a cutoff radius for each type of atom, allowing for the transferability and scalability of NNPs. In particular, the introduction of the "active learning" or "query by committee" scheme facilitates the efficient sampling of PES and enhances the effectiveness and transferability of NNPs. Active learning has been an indispensable component in the recent development of NNPs. ^{31,44}

Whereas MLPs empower rapid advances in MD simulation, significant challenges exist in their widespread use due to the limitations in describing long-range interactions with atom-based descriptors⁴⁵. Previous studies of NNPs are mostly focused on bulk systems^{46,47}, including liquid water^{48,49} and dilute solutions of small molecules⁵⁰. Much less attention was given to inhomogeneous systems such as water near an interface or in confined geometry. In comparison with bulk systems, liquid water at inhomogeneous conditions has more complicated atomic configurations and PES, rendering a greater challenge for training MLPs. Currently, there are only several studies applying NNPs to water at solid-liquid interfaces^{51–53}, such as liquid water at the surfaces of ZnO^{54,55} or alloys⁵⁶ and nanoconfined water^{57,58}. These studies provide valuable insights into unique challenges in using NNPs for inhomogeneous molecular systems.

In this work, we explored the transferability of NNPs for predicting the interfacial properties of liquid water near graphene surfaces. Two deep potential (DP) models, Model S and

Model F, were constructed using the DP-GEN (Deep Potential Generator) scheme⁴² to represent the PES and label the reference data. DP-GEN is a concurrent machine learning method similar to active learning⁴² except that it requires sampling unlabeled data⁵⁹. The DP descriptors are obtained from the embedding neural network of the DP models and compared with those commonly used in the works of literature including SOAP²⁶ and ACSF⁶⁰. We find that the trained DP descriptors have excellent representational power in characterizing the chemical environment of the atoms. They could conceivably be acted as general molecular representations for a variety range of downstream tasks or be in combination with other MLPs as their input, not just for constructing DP models. Subsequently, the transferability of the two DP models were tested with systems of different sizes by comparing their predictions for energy and atomic forces with the DFT calculations. We then compared in detail the relevant statistical results of DPMD and classical MD simulations for systems at different temperatures, including O atoms density distribution and radial distribution, to better complement the assessment of the DP model transferability.

Models and Methods

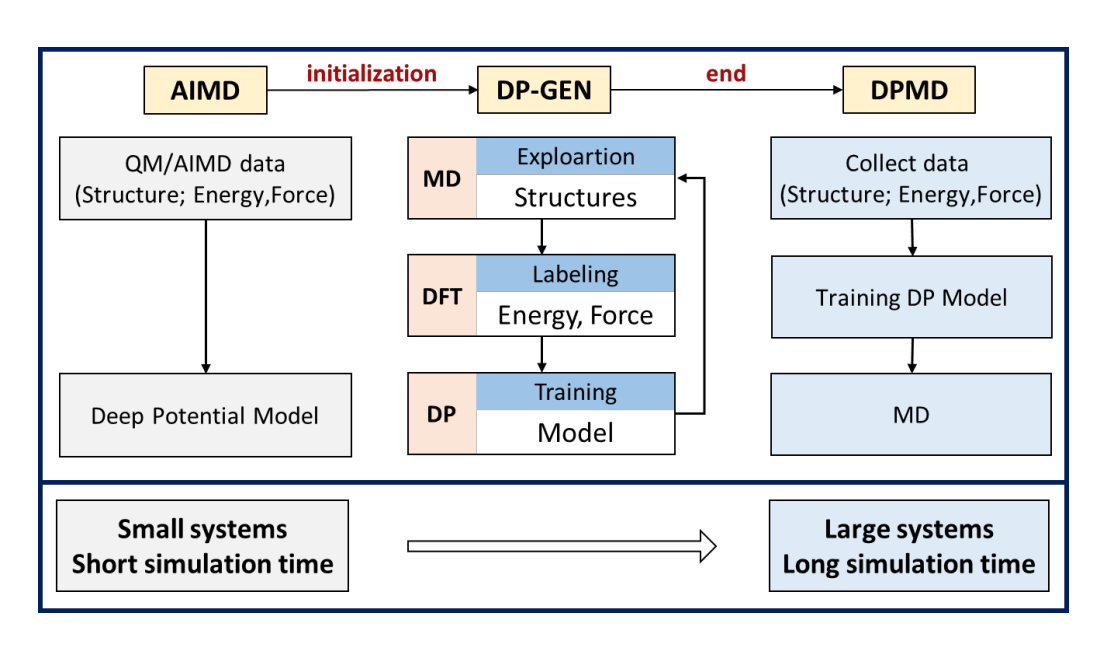


Figure 1. Schematic flow chart for training a DP model with AIMD and DP-GEN for DPMD simulation. The procedure includes three parts: AIMD for generating the initial trajectories, DP-GEN for enriching the dataset, and DPMD for large-scale simulation. The DP model extends short-time AIMD for small systems to long-time DPMD for large systems.

Computational scheme. Figure 1 outlines a three-step workflow implemented in our deep potential (DP) molecular dynamics (DPMD) simulation. The DP training starts with a dynamic trajectory generated by AIMD with the initial data for atomic positions, configurational energies, and atomic forces. Next, we adopt the DP-GEN scheme to enrich the dataset by generating additional configurations⁴². Finally, all data are collected to train the DP model, including the initial data provided by AIMD and the data obtained by sampling, before it is used to simulate large systems. In the DP-GEN step, MD and DFT calculations are carried out iteratively through structural exploration, labeling, and training. In the exploration stage, we conducted DPMD simulations to sample new configurations (viz. atomic structures) or to select certain simulation frames for labeling with atomic forces and system energy. According to the simulation protocol of DP-GEN, we performed parallel MD simulations with four DPs that are trained with the same dataset and optimization methods but with different random seeds in initializing the network parameters⁴². We used the standard deviation computed from the ensemble averages of the above four DPs as the criteria to select the structures of interest. Specifically, the standard deviation ϵ refers to the maximum of that corresponding to the atomic forces F_i predicted by the four DPs

$$\epsilon = \max_{i} \sqrt{\langle \| \mathbf{F}_{i} - \langle \mathbf{F}_{i} \rangle \|^{2} \rangle} \tag{1}$$

where the subscript i denotes the atomic index, and $\langle ... \rangle$ represents the ensemble average over the four DPs. The parallel DPMD simulations would yield consistent results if the dataset is sufficiently large for training the DP models. Otherwise, the non-convex nature of the neural

network implies that the four DP models would predict different results owing to the different random seeds. Therefore, the parallel DPMD simulations allow us to retain the atomic structures with proper standard deviations and discarded structures that are too similar or differ too significantly from the structures in the previous round training dataset. In labeling the selected structures, we carried out DFT calculations to evaluate the total energy of the system and atomic forces for each frame. Next, we performed the DP training based on the enriched dataset that includes both the DP-GEN data and the original dataset. Parallel DPMD simulations are then carried out to generate new trajectories for the next iteration until the convergence. After the iterative cycles in training the DPs, the DPMD simulation reflects atomic interactions underlying both the initial dataset from AIMD and the sampling datasets from DP-GEN. More information about DP-GEN, including sampling criteria and iteration details, can be found in Section 1.C of Supplemental Material.

AIMD simulations. AIMD simulations were applied to two systems: system I consists of liquid water and a graphene sheet, and system II is pure liquid water. For both systems, the results from AIMD provide the initial dataset for implementing the DP-GEN scheme. Figure 2 presents snapshots of these systems for AIMD or DPMD simulations. The simulation box for system I contains 57 water molecules and has the dimensions of $12.28 \times 12.76 \times 15.00$ Å in x, y, and z directions, respectively, with a graphene sheet consisting of 60 carbon atoms positioned at the z=0. In system II, the simulation box contains 64 water molecules and has the dimensions of $12.42 \times 12.42 \times 12.42$ Å, which mimics liquid water with a bulk density of 998.8 kg/m^3 . All AIMD simulations were conducted by using the Quickstep program from the cp2k package 61.62. The periodic boundary conditions (PBC) were imposed in the x, y, and z directions. Accordingly, system I is equivalent to a thin film of liquid water confined between two parallel graphene sheets

that are infinite in the *x-y* plane. For both systems, AIMD simulations were carried out at a series of temperatures in order to explore the PES with a short duration of the simulation time⁶³. More details about AIMD simulations are available in Section S1.B of Supplemental Material. The AIMD dataset consists of 9003 frames of configurations for system I and 9002 frames for system II, from which we chose a certain number of frames to build the initial training dataset for the DP-GEN iteration. The performance of the DP model is relatively insensitive to the initial dataset from AIMD and it is much smaller than the enriched dataset established by the subsequent DP-GEN exploration.⁶³

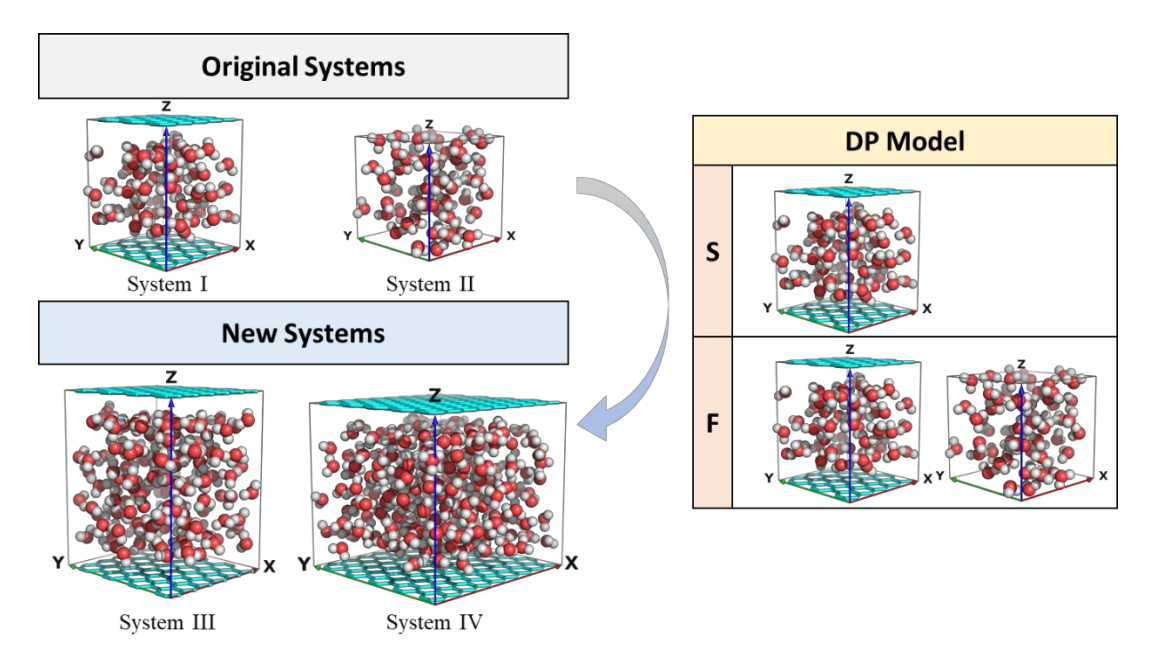


Figure 2. Four systems investigated in this work with AIMD and DPMD simulations. System I and II refer to original systems simulated with AIMD for generating the initial training dataset; System III and IV refer to larger systems that are used to evaluate the transferability of the DP models. Two types of DP models, Model S and Model F, are distinguished by the training dataset for system I and for systems I and II, respectively.

Construction of the DP models. Like other neural network potentials (NNPs), locality approximation is used in constructed the DP models⁵⁸. The total energy of the system is expressed as the sum of neighboring atomic energies

$$E = \sum_{i} E_{i} \tag{2}$$

where E_i is the energy of atom i. In evaluating the neighboring atomic energies, a cutoff distance of 6 Å is adopted with a smooth function applied at 5.5 Å. Consequently, the chemical environment for each atom is defined by atoms within the cut-off distance.

In the smooth version of the DP model⁶⁴, the neural network contains two components: the embedding neural network and the fitting neural network. The former is designed to preserve the translational, rotational, and permutation symmetries of the system under investigation; it maps the chemical environment of each atom, *i.e.*, the identity and coordinates of the neighboring atoms, to self-adapted descriptors. The fitting neural network establishes correlations for the energies and atomic forces of the system in terms of the self-adapted descriptors. It's worth mentioning that the energy and atomic force used as initial input for the fitting neural network are calculated from the first principles methods such as electronic DFT. Both embedding and fitting networks are optimized with the Adam method by minimizing the loss function^{27,64}

$$Loss = \frac{p_e}{N} \Delta E^2 + \frac{p_f}{3N} \sum_{i} |\Delta F_i|^2$$
(3)

where ΔE and ΔF_i denote the root mean square (RMS) errors in energy and force, respectively. The factors p_e and p_f are tunable during the training process. More details about the configurations of the DP model can be found in Section S1.A of Supplemental Material. As shown in Figure 2, we constructed two types of DP models, Model S and Model F, based on whether to incorporate the data from the bulk system (System II).

Assessment the DP Transferability. The enriched dataset, *i.e.*, the data from DP-GEN sampling plus the original dataset from AIMD, are used to train an ensemble of four DPs that differ only in the initialization parameters. These DPs are then applied to the larger systems by DPMD simulations. The performance of different DPs can be measured with the relative force model deviation defined as

$$E_{f_i} = \frac{\left|\epsilon_{f_i}\right|}{\left|f_i\right| + l} \tag{4}$$

where f_i represents the force on atom i, ϵ_{f_i} stands for the corresponding standard model deviation, and l=1 eV/Å is a constant introduced to ensure that an atom with a small absolute model deviation will also have a small relative model deviation⁶⁵.

To test the transferability of the DPs, we constructed two new systems, systems III and IV as shown in Figure 2, which are larger than those used for training the DP models. System III contains 96 carbon atoms and 141 water molecules, and the simulation box has the dimensions of $14.74 \times 17.02 \times 20.66$ Å in x, y, and z directions. System IV consists of 180 carbon atoms and 276 water molecules in the simulation box of size $22.11 \times 21.27 \times 20.00$ Å. We evaluated the transferability of two DP models, Model S and Model F, as explained in Figure 2, by analyzing the atomic forces and energies predicted by DPMD for systems III and IV at different temperatures (300K, 400K, and 500K). Sections S1.C and S1.D of Supplemental Material detail the simulation setup and the DP-GEN iteration process for training the DP models used in Model S and Model F.

Results and Discussion

In this section, we first discuss DP descriptors for the characterization of the atomic chemical environments with Model S and Model F and analyze the two models' performance in reproducing the first-principles results. Next, we evaluate the accuracy and transferability of

different DP models by examining their applicability to systems larger than those considered in the training dataset.

DP descriptor vs. SOAP and ACSF

As mentioned above, the training of DP models has two components, the embedding neural network, and the fitting neural network. The embedding network is designed to construct the descriptors to represent the chemical environment of individual atoms based on the spatial coordinates of the neighboring atoms. Many descriptor construction methods have been proposed for the development of atomistic machine learning force fields, including the Coulomb matrices⁶⁶, Many-Body Tensor Representation (MBTR)⁶⁷, Atom-Centered Symmetry Functions (ACSF)⁶⁰, Smooth Overlap of Atomic Positions (SOAP)²⁶. In this work, we compare the ACSF and SOAP descriptors with the DP descriptors used in the construction of Model S and Model F. The analysis is based on one specific structure randomly selected from system I. As shown in Figure S5, this structure has 231 atoms, including 60 C atoms, 57 O atoms, and 114 H atoms. The descriptors used here are two-dimensional arrays, whose row denotes the number of atoms in the system and col denotes the number of features of the method. And therefore, the size of the descriptors from different methods can all be expressed as 231*col, where the col varies greatly between these methods. The configurations of embedding network in Model S and Model F are the same and the descriptors have the same shape. The shapes of DP Model, SOAP and ACSF descriptors are (231,1600), (231,2100) and (231,36). There are some custom settings affecting the dimension of the feature in SOAP and ACSF, which can be found in S1.E part of Supplemental Material.

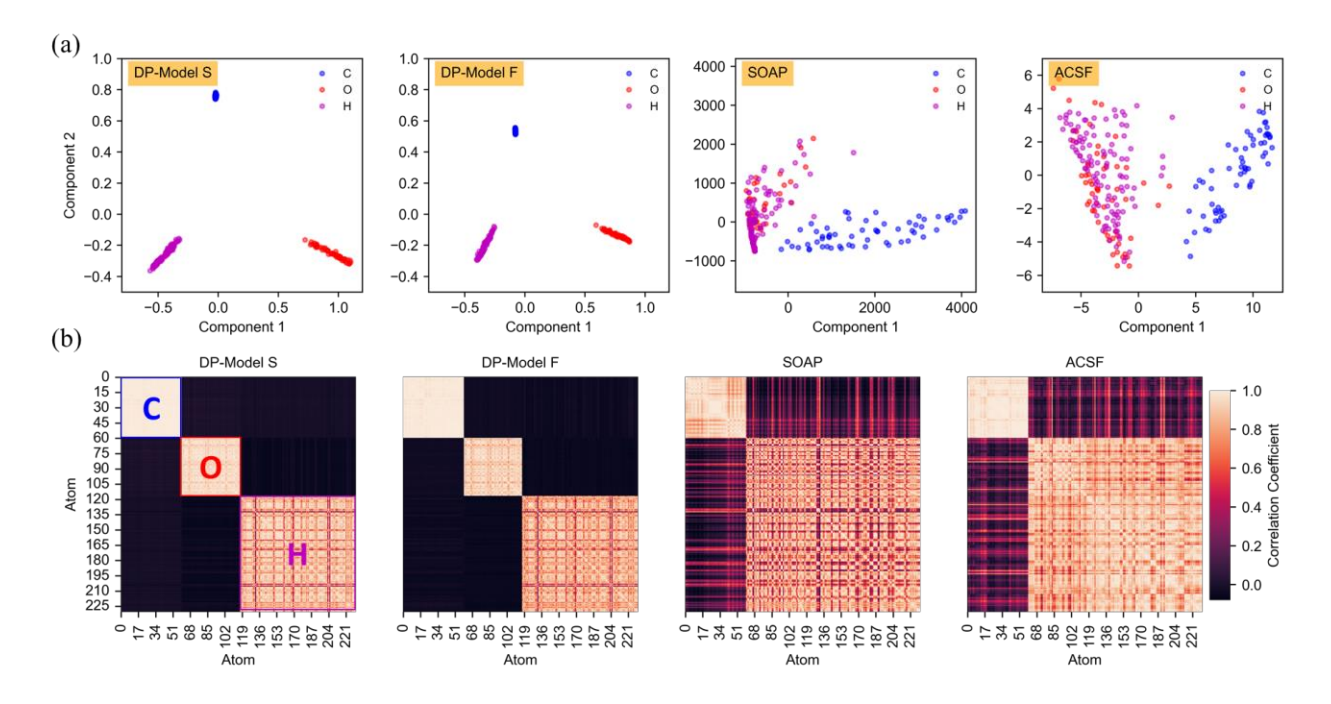


Figure 3. (a) The graphical representation of the descriptors after the dimension reduction. From left to right, they correspond to Model S, Model F, SOAP, and ACSF. In this diagram, the blue points are affiliated with the coordinates of C atoms, the red points for O atoms, and the purple points for H atoms. (b) The corresponding correlation matrix of the descriptors. Light color represents a high correlation coefficient, and dark color represents a low correlation coefficient. The first diagram on the left, for example, shows the positions of C, O, and H atoms.

Figure 3a compares different descriptors based on the principal component analysis (PCA). Each point in this diagram represents the coordinates for one type of atoms (viz., blue for C atoms, red for O atoms and purple for H atoms). The graph can be analyzed in terms of the inter-class and intra-class distances at two levels, *i.e.*, the way how the same atoms are aggregated and the differences between the presentation of different atoms. The descriptors given by Model S and Model F perform better than SOAP and ACSF as evidenced by the clustering of the same atoms and the separation of different atoms. The SOAP and ACSF descriptors distinguish only C atoms from other atoms while the O and H atoms are mixed together. Besides, the distribution of atomic

characteristics shows no regularity as far as the same types of atoms are concerned. Because the C atoms are all located on the graphene sheet, the differences in the local chemical environments of water molecules are mainly reflected in the distance from the graphene surface as represented by the DP descriptors. To show these differences graphically, we present the corresponding correlation matrices of the DP descriptors in Figure 3b. Each matrix element manifests the correlation coefficient of two atomic descriptors. For example, the ij element in the correlation matrix denotes the correlation coefficient of the atomic descriptor with index i to that with index j. Figure 3b indicates that there is no correlation between different atom species for the DP models. However, the SOAP and ACSF descriptors are partially correlated between different atomic species, especially between O atoms and H atoms. Therefore, the DP descriptors are more likely to give a good representation of the chemical environments of individual atoms. As noted in Section S1.E of Supplemental Material, SOAP and ASCF descriptors are constructed directly from the coordinates of the atoms and are readily available from standard software packages. By contrast, the DP descriptors are extracted from the embedding net and must be trained using known labels. So just from the standpoint of characterizing the chemical environment, it's not surprising that DP descriptor works better than the other two, as it is trained and costs more. Even though, the great performance of the DP descriptors demonstrates their feasibility and potential applications in atomic-scale modeling⁶⁸ not just for constructing deep potential or conducting DPMD simulations.

Accuracy of the DP models

In this subsection, we compare the energies and atomic forces predicted by the DP models with the DFT results that are not included in the training dataset. Figure 4 presents the predictions of Model S and Model F for the system energy and the atomic force, that is, the force on each

atom, in the x-direction (force x) in systems I and II. Similar results can be obtained for the atomic forces in the y and z directions, as shown in Figure S6.

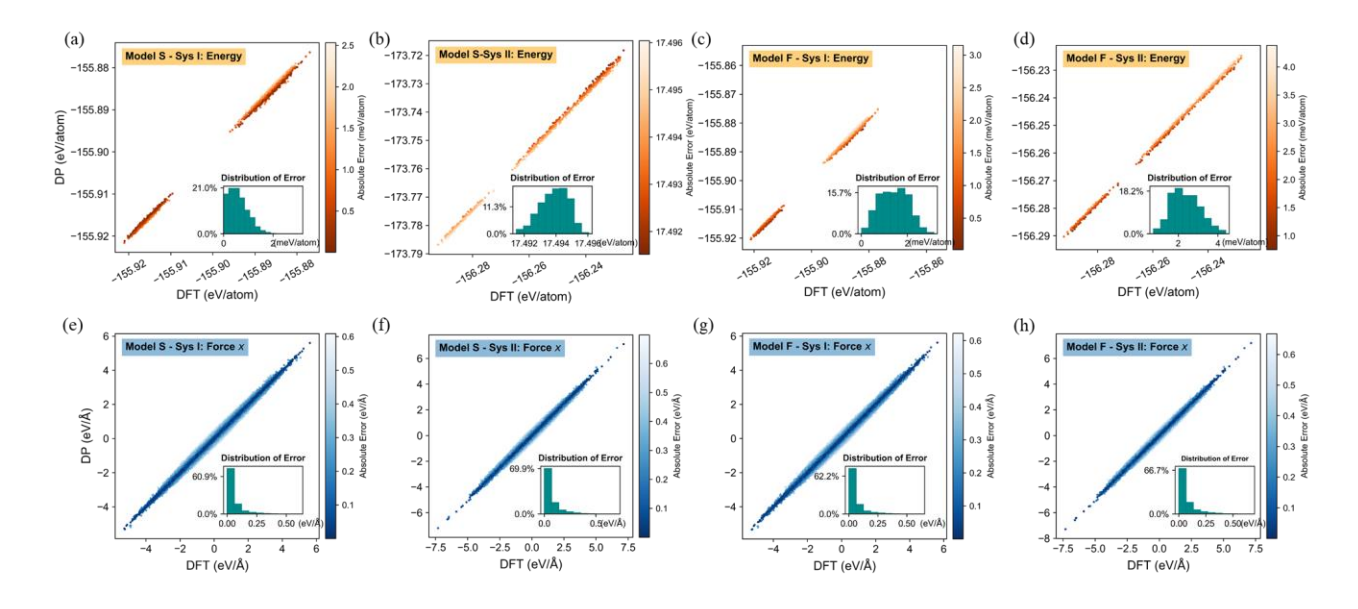


Figure 4. The comparison of the energy and *x*-direction atomic forces (force *x*) predicted by the DP models and DFT calculations. The first and second rows correspond to the energy and force *x* for each atom respectively; a, b, e, and f are the results from Model S; c, d, g, and h are the results from Model F.

Table 1. The RMSE of energy per atom and force *x* of individual atom between DFT calculations and the DP models.

Model	Sys I-RMSE		Sys II-RMSE	
	Energy/atom(meV)	Force (eV/Å)	Energy/atom (meV)	Force (eV/Å)
S	0.698	0.0798	17494	0.1005
F	1.547	0.0794	2.458	0.0995

As mentioned above, the training datasets for Model S and Model F are different. The former contains only the atomic structures from system I (viz., graphene in water), while the latter contains the atomic structures from both systems I and II (viz., graphene in water and pure liquid

water). In terms of chemical environment, the training datasets for Model S are more uniform than Model F, and the similarity in the atomic characteristics of the training data explains why Model S is superior to Model F for reproducing the atomic energies and forces for system I. As shown in Figure 4a and 4c, Model S predicts the energy per atom in system I more accurate than Model F. Table 1 shows that the RMSE predicted by Model S is 0.698 meV, much less than 1.547 meV predicted by Model F. As for the atomic force predictions, we observe only small differences between the two models as shown in Figure 4e, 4f, and Table 1. It is probably worth mentioning that 1 eV equals 23.06 kcal/mol and that the above energy errors are much less than the chemical accuracy, 1 kcal/mol.

For system II, the relative performance of the two DP models is reversed, that is, Model F predicts the atomic energies and atomic forces more accurate than Model S. Especially, Table 1 indicates that Model S predicts the RMSE of atomic energies up to 17.49 eV, higher than 2.458 meV predicted by Model F by almost 4 orders of magnitude, which looks more like a systematic bias. However, the RMSE for force *x* predicted by Model S is very close to that by Model F. The disparities in Model S and Model F can be attributed to their different training datasets. The atomic structures of water molecules in system I and system II are different, representing the confined water and bulk water respectively. Unlike Model F, Model S does not include any atomic structure from system II in the training dataset. As a result, it may not fully capture the local chemical environment of the bulk system. For example, system I contains only a portion of "bulk" water molecules with no C atoms within their truncated radius, meaning that the chemical environment of these water molecules is similar to that of the bulk water. We may identify those O atoms with no C atoms in their chemical environment in the training dataset for system I and compare the O-O and O-H radial distribution functions (RDFs) with those from system II as illustrated in Figure

S7a and S7b. While the RDFs of O-O and O-H pairs have a similar shape in system I and system II, the numbers of neighboring O and H atoms within the O-atom truncation radius are noticeably different (Figure S7c and S7d). Compared with the O atoms farthest away from the graphene carbons in system I, those O atoms in the bulk (system II) have more H atoms within their cutoff radius. In other words, the chemical environments for the O atoms in system I are significantly different from those in the bulk water even when they are in the middle of the graphene layers. In this work, the size of the simulation box is 15 Å in the z-direction. Because the cutoff radius for the chemical environment of O atoms is set to 6 Å and the van der Waals radius of C atom is approximately equal to 1.7 Å, the O atoms in the confined system are distinctively different from those in the bulk even when they are located in the middle plane between graphene sheets, which contradicts the locality assumption. The above analysis indicates that the local environment of water molecules in system I is quite different from that of bulk water (system II). Unlike atomic forces, there is only one energy label for each frame (viz., atomic configuration). While the former has three components of force labeled for each atom (in x, y and z directions). In addition, the total energy depends on the positions or the local environments of all atoms. In other words, each component of the atomic force is a local property but the energy is a global property⁶⁹. Although the DP model adopts the locality approximation with the total energy of the system expressed as the sum of atomic energies, there is no so-called atomic energy label and the model cannot decompose the energy properly. It only ensures that the overall energy is accurate. Because the total energy contains contributions from both graphene and water molecules in the training data, Model S predicts the atomic forces accurately but is not able to predict the total energies of different systems. Conversely, the training dataset of Model F contains the atomic structures of both systems I and II thus can predict both the energy and force of similar systems. Owing to these

two systems having different atomic structures, the data consistency of Model F is not as good as that of Model S, that is, the former training data contain richer features. As a result, Model F does not converge as efficiently as Model S in training the DP models. The differences in convergence are also reflected in the RMSE values of the energy and atomic forces for system I predicted by Model S and Model F (Table 1).

DP Models Transferability

Transferability is an important measure of the usefulness of the neural network potentials (NNPs). Ideally, the NNP model trained with the first-principles calculations for small systems should be applicable to larger systems. To test the transferability of our DP models, we consider liquid water-graphene interface systems with the larger size than system I (viz., system III and IV shown in Figure 2). Then Model S and Model F were tested with 5 ns DPMD simulations in the NVT ensemble for system I, III and IV at 300K, 400K and 500K. A total of eighteen DPMD simulation runs, using the two types of DPs models (S and F) for the three systems at three temperatures (2×3×3), were used to evaluate the transferability of the DP model in terms of the relative deviations of atomic forces and system energy.

The relative deviation of atomic forces. As explained in the Method, this metric is calculated from the force predictions for the same atomic structure but with an ensemble of 4 DPs that differ only by the initial parameters. Different structures were generated with the DPMD simulations with one of the four DPs while other three DP potentials from the ensemble are included to evaluate the model deviations. For simplicity, we first analyze the DPMD simulations for systems I and III.

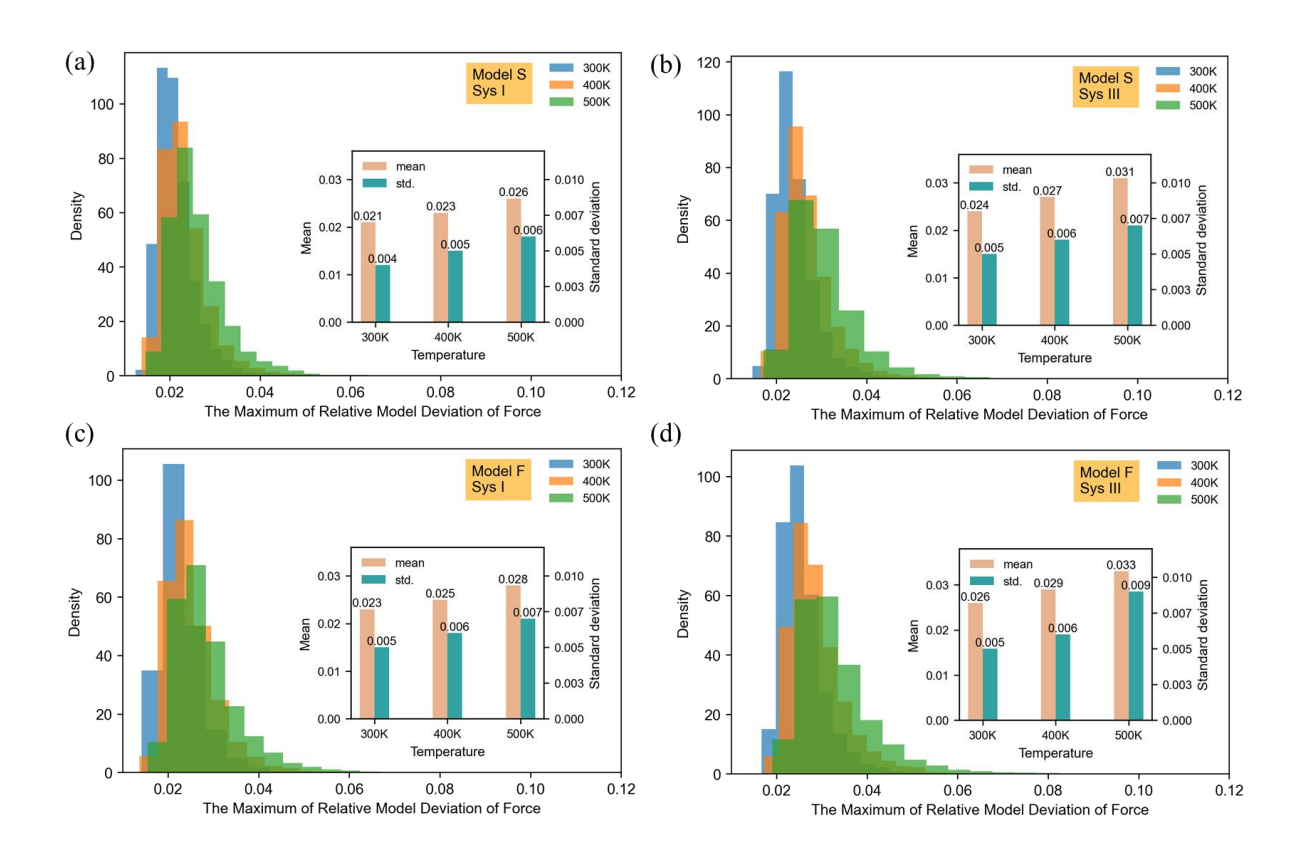


Figure 5. The histogram of the relative model deviation of the atomic forces of system I predicted by an ensemble of four DPs for Model S (a) and Model F (b). The histogram of the relative model deviation of the atomic forces of system III predicted by an ensemble of four DPs for Model S (c) and by an ensemble of four DPs for Model F (d). The inset subplots give the mean value and standard deviation at different temperatures.

Figure 5a and 5b show the relative model deviations of the atomic forces for systems I and III predicted by Model S and Model F, respectively. The insets present the mean values and standard deviations at different temperatures. Figure S8 shows the variation of the relative deviations of atomic forces over the duration of simulation. In all cases, both the mean value and standard deviation of the atomic forces grow with temperature because of the enhanced thermal fluctuation. As aforementioned, system I corresponds to the initial system that generates the training data. System III has more water molecules and larger spacing in the *z* direction thus with

a different degree of confinement and chemical environments. At a given temperature, the relative deviation of atomic forces in system I is smaller than that of system III. However, the differences are relatively small (no more than 10%). Based on the force criterion alone, it seems that Model S is transferable to larger systems.

To study whether a small relative model deviation in atomic forces is enough to justify the transferability of the DP model, we selected 50 atomic structures of system III at equal intervals from the DPMD simulation at 300K and calculated the potential energy and atomic forces with DFT for each structure. The results were compared with those predicted by Model S. Figure 6a and 6b present the corresponding comparisons for the potential energy and atomic force x, respectively. And the comparisons for atomic force y and z can be found in Figure S9. It can be found that the error of total energy per atom is up to 5.2 eV/atom, much larger than the prediction error of Model S for the test dataset shown in Figure 4a. In contrast, the atomic forces predicted by the DP model are in excellent agreement with the DFT results. In fact, it can be found the case is consistent with the performance of Model S for system II in the test dataset, that is, bad energy prediction but good force prediction by the DP model. As a control, we also analyzed the DPMD simulation results for systems I and III with Model F. Figure 5c and 5d present the relative force model deviations, and Figure 6c and 6d compare the DFT calculations and the corresponding results predicted by Model F for the total energy per atom and atomic force x. As can be seen from Figure 5, the model deviations of Model S and Model F are comparable, seeming to imply the similar accuracy for the prediction of the DP models for system III. However, Figure 6 shows that Model S is subject to a larger deviation in predicting the potential energy of system III than Model F. For both models, we also compute their model deviation of energy per atom and atomic forces of the above 50 structures from system III. As shown in Figure 7a, Model F yields small model

deviations of both energy and force. Conversely, Model S shows a larger deviation of the total energy per atom while a smaller deviation for the atomic forces. In other words, Model S can accurately predict the atomic forces but not the system energy. Therefore, combining the model deviation of energy per atom and atomic force is more indicative of how well the model predicts one structure.

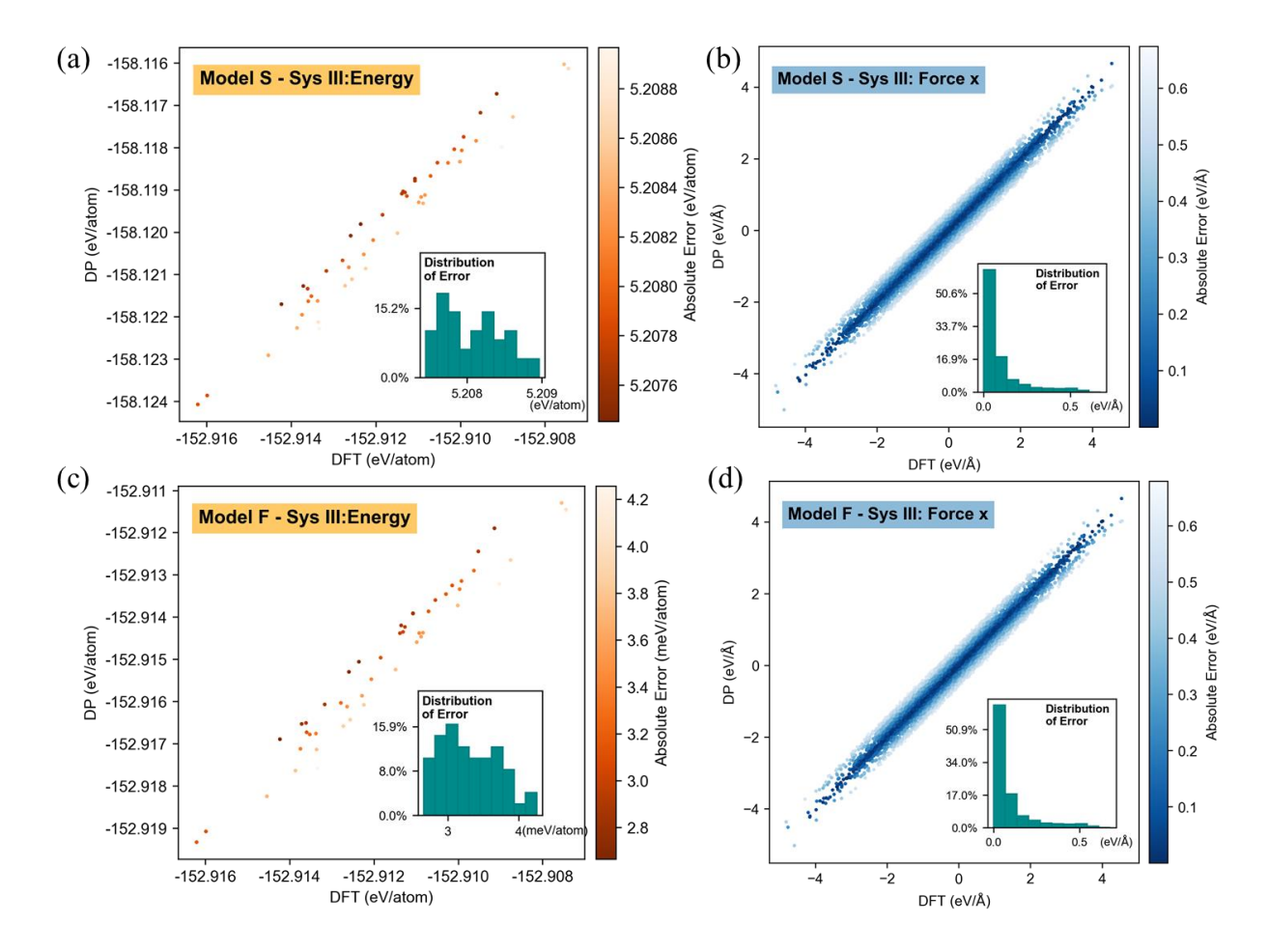


Figure 6. The comparison of the potential energy and atomic force *x* predicted by DFT and the DP models, i.e., Model S (a,b) and Model F (c,d) for system III.

The above analysis indicates that using the model deviation or relative model deviation of the atomic forces alone is not necessarily an indicator of whether the model can predict the energy accurately. There is little correlation between the predictions of energy and atomic forces especially when we consider the transferability of the DP models for systems with different local chemical environments. Perhaps a more suitable criterion is to introduce model deviations of both energy and atomic forces into the evaluation steps. Specifically, this can be done by comparing the model deviation with the RMSE of the model on test dataset. If the model deviations are significantly less than the corresponding RMSE for both total energy and atomic forces, the DP model would have good transferability. This can be seen by comparing the data in Table 1 and Figure 7. For example, the model deviation of energy per atom of Model S is 186.2 meV, much greater than the corresponding RMSE of Model S on the test dataset of system I, *i.e.*, 0.698 meV, implying that the model S cannot yield an accurate energy. Similarly, the model deviation of atomic forces of Model S is 0.0443 eV/Å, less than the corresponding RMSE, *i.e.*, 0.0798 eV/Å, showing that the model S can predict the atomic forces well. For Model F, the model deviation of energy per atom and atomic forces are 0.3 meV and 0.0465 eV/Å, less than their corresponding RMSE on the test dataset, 1.547 meV and 0.0794 eV/Å.

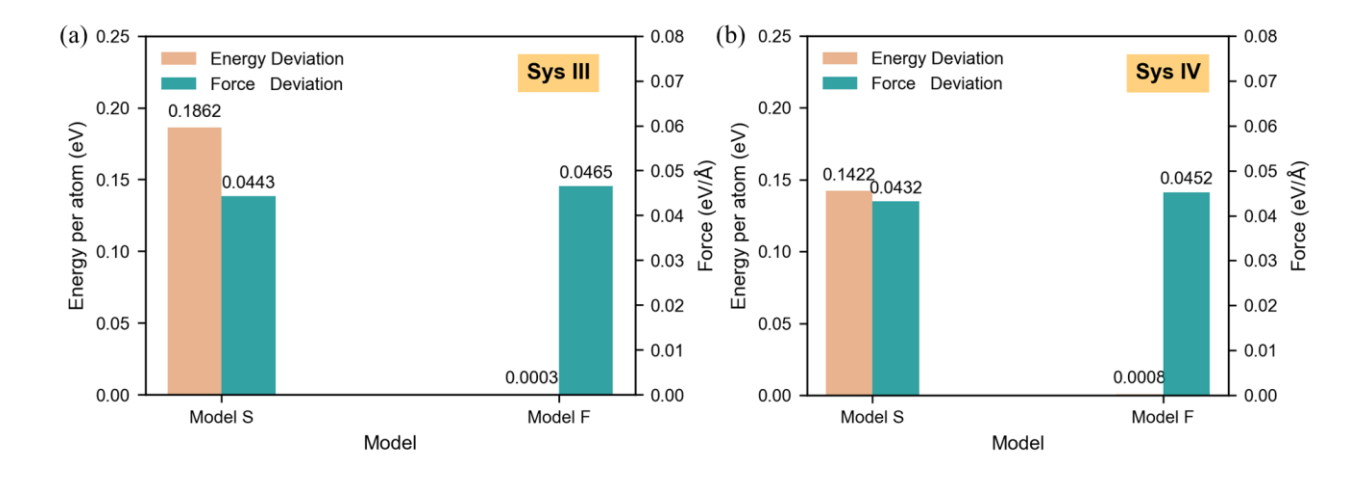


Figure 7. The model deviation of energy per atom and atomic force of the selected structures from system III (a) and IV (b) for Model S and Model F.

To validate the above criterion, we selected 50 atomic structures at equal intervals from DPMD simulations of system IV at 300K and compared the DFT calculations and DP predictions.

Since there are more atoms in system IV, DFT calculations could not achieve convergence for 15 structures so that they were discarded and the remaining 35 structures were used in our analysis. It can be seen from Figure 7b and Figure S10 that the situation is similar to that of system III discussed above, *i.e.*, the model deviations of energy per atom and atomic forces predicted by Model F are less than the corresponding RMSEs. Therefore, we assert that Model F can give the accurate predictions of the system energy and atomic forces, while Model S does not. From these analyses, we conclude that the transferability of Model S is inferior to that of Model F.

Based on the combined criterion of energy and force evaluations, we selected 200 structures at equal intervals from the DPMD simulations of model F at different temperatures for three different systems, *i.e.*, system I, III and IV. Figure S11 shows the corresponding model deviations for the energy per atom and atomic forces. Both the model deviation of energy per atom and atomic forces are less than the corresponding RMSE shown in Table 1. It seems that we can therefore conclude that Model F is able to achieve good transferability at different temperatures for different systems.

Further Illustration of Model F Transferability. The previous parts have evaluated energy and atomic forces for randomly selected structures from system III and IV, showing that Model F can achieve accurate predictions of energy and atomic forces for the new systems. As far as transferability evaluation is concerned, although it's essential and adequate to pay attention to the energy and atomic forces of the system, it's specific to a certain configuration or individual, without considering the statistical related properties. As mentioned at the very beginning, the advantage of MLP is its ability to perform long time molecular dynamics simulations with the first-principle accuracy at a lower cost. Therefore, we analyzed the relevant statistical properties

of the DPMD simulations to provide a complementary account on the transferable ability of the DP models.

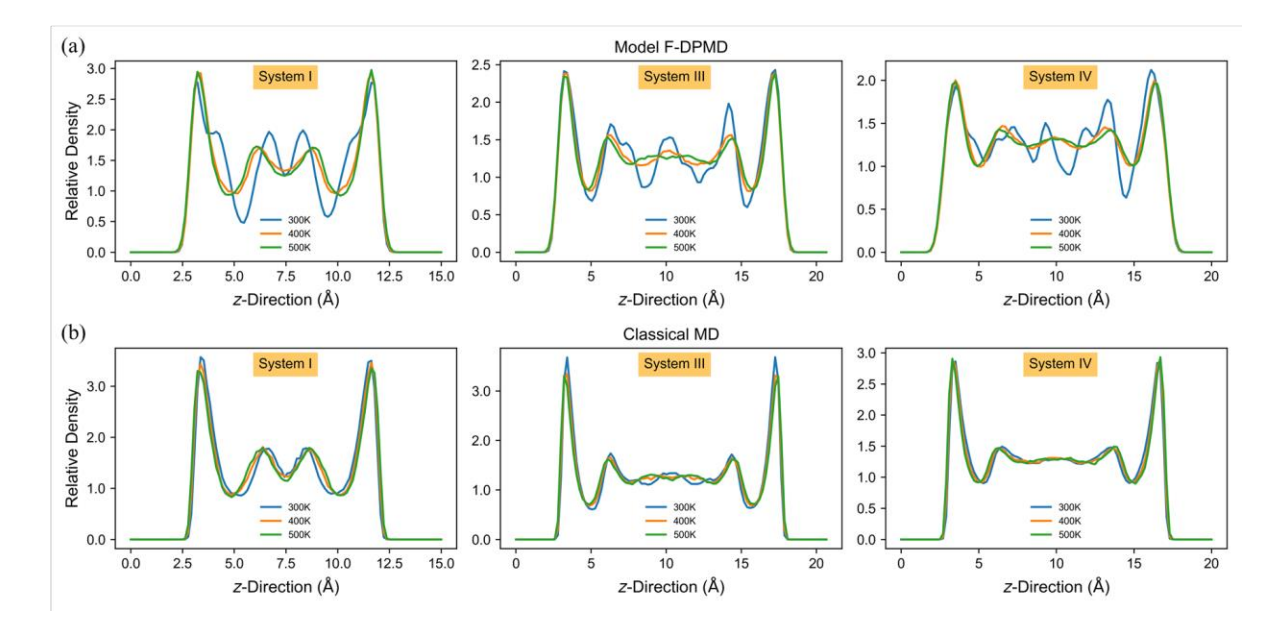


Figure 8. The density distribution of O atoms along the z-axis of different systems at 300K, 400K and 500K in DPMD simulations (a) and classical MD simulations (b).

As mentioned above, we carried out eighteen DPMD simulation runs, using Model S and F for the system I, III and IV at 300K, 400K and 500K. First, we investigated the change in the potential energy (PE) of systems with time. As shown in Figure S12, after a relatively short period of time, almost all the systems' potential energy tends to fluctuate at a constant value, except the simulation of system IV at 500K conducted by Model S. This is in line with the conclusion that has been reached that Model S doesn't transfer well. In general, much richer exploration for potential energy surface can be achieved in the longer time simulations of larger system at higher temperature. And such exploration tests the transferability of MLP models. For example, the simulation of system IV at 500K conducted by Model S didn't remain stable. This also shows that the stability of some simulations does not indicate that the model has reliable transferability, for example, although Model S gave stable simulations of system III at different temperature, its

predictions of the energy were inaccurate, as shown in Figure 6a. In contrast, Model F could make accurate energy and atomic forces predictions and possesses good transferability. Accordingly, the simulations based on Model F all maintain a steady state of potential energy.

Next, we only focused on simulations conducted by Model F and omitted Model S-based simulations. Specifically, we analyzed the density distribution of O atoms in the *z*-axis direction, as well as the RDFs of O-O and O-H. To better illustrate these DPMD simulation results, we also have preceded 5 ns NVT ensemble classical MD simulations of the above systems using GROMACS program⁷⁰. The simulation procedures and force filed parameters used are consistent with this work⁶² and will not be described in detail here. It should be added that we fixed graphene in the classical MD simulations because the force field parameters of C atom used here are not accurate enough to model the flexibility of graphene well.

Figure 8a and 8b present the density distribution of O atoms along the z-axis for the different systems in the DPMD simulations and classical MD simulations, respectively. Due to confinement effect, the density distributions of O atoms show symmetrical layer structure along the z-axis. And in DPMD simulations that is more clearly stratified at 300K compared to the distributions at 400K and 500K. In contrast, the results at different temperatures in classical MD simulations differ insignificantly. We think that this is related to portrayal of the interactions by the two types of simulations. The water molecule in classical MD simulations is TIP3P⁷¹ model with fixed conformation, and the graphene is also fixed. Furthermore, the force field description is not accurate as in DPMD simulations, so the interactions described by classical MD are not as complex and fine as in DPMD. And this is more pronounced at lower temperature due to the random perturbation of the kinetic energy. Notice that the density distribution of O atoms for system IV in DPMD simulation at 300K shows an asymmetric structure. We suggest that this

related to the flexibility of graphene. Specifically, we examined the density distribution of C atoms along the z-axis as shown in Figure S13 and here we placed the graphene in the middle. It can be found that the graphene is not always in a fixed plane, but fluctuates back and forth in the z-axis direction; on average, the graphene tends to be on the left side. And the layered structure of O atoms closer to that side is more pronounced, which is also related to the confinement effect.

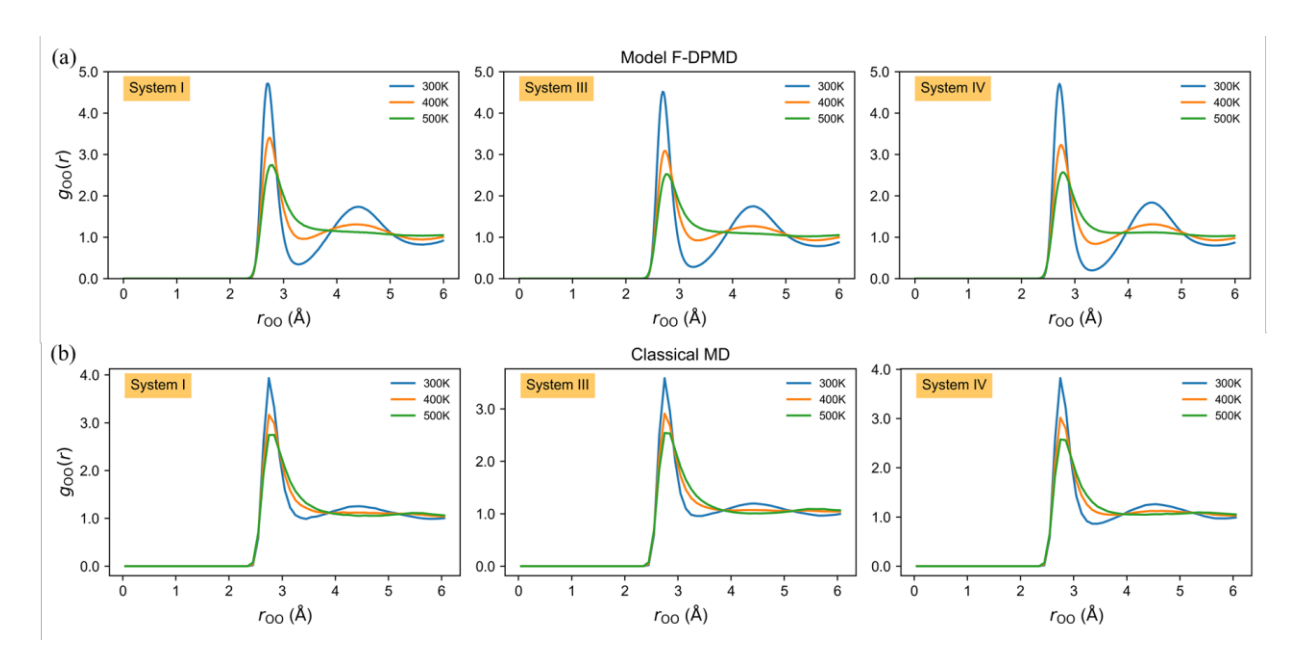


Figure 9. The RDF of O-O for different systems in DPMD simulations (a) and classical MD simulations (b) at 300K, 400K, and 500K. And from left to right are system I, III and IV.

Then we calculated the radial distribution functions (RDF) of O-O and O-H, that is g_{00} and g_{0H} , for different systems in DPMD and classical MD simulations as shown in Figure 9 and Figure S14 respectively. For g_{00} in Figure 9, the first peak represents the length of the hydrogen bond formed between the central O atom and the O atom of adjacent water molecule, which is close in both DPMD and classical MD simulations. At higher temperatures, g_{00} only exhibits a structure feature in the region closer to the central atom, and the further away from it, g_{00} is closer to 1. This is due to the kinetic energy randomly perturbing the intermolecular interactions and thus

showing a more homogenous feature. Overall, the structured character of g_{00} in the DPMD simulations is more pronounced, especially at 300K. This is still in that DPMD could portray intermolecular interactions more precisely with the precision of the first principle calculation, unlike the conformation of fixed water model in classical MD simulations. In the same way, we analyzed the RDF of O-H, g_{OH} , as shown in Figure S14. It differs form g_{OO} and exhibits multiple peaks. The first peak means the O-H bond of the water molecule, the second peak represents the distance between the H atom in donor hydroxyl group and the acceptor O atom, and the third peak is the distance between the acceptor O atom and another H atom in the donor water molecule. Overall, g_{OH} shows a similar pattern to g_{OO} at different temperatures and in two types of simulations and this will not be developed in detail here.

In summary, the above further illustrates the good transferability of Model F through change in potential energy of the systems and some statistical properties. This suggests that we can show whether the model is able to transfer well by comparing the model deviation in energy and atomic forces with the model's RMSE on the test set, thus not relying on costly DFT computational validation. This is particularly true for large systems, because DFT calculations can no longer be effectively performed here.

Conclusion

In this study, we have constructed DP models based on the high precision data generated from AIMD and the DP-GEN scheme for liquid water near a graphene surface and in the bulk. We tested the transferability of these models through the static structure calculations of the total energy and atomic forces in systems larger than those used for training the DP models. We compared the DP descriptor with the classical descriptors such as ACSF and SOAP. We find that the DP descriptor obtained from training is superior to classical descriptors in characterizing the chemical

environment. In addition, the relative force model deviation alone offered by deepmd-kit package²⁷ is not a good indicator of whether the DP model can predict both energy and atomic forces accurately. A feasible alternative is to incorporate both the model deviations of energy and atomic forces into the evaluation step. Furthermore, when evaluating the transferability of a DP model, we should compare both the model deviations for the system energy and atomic forces with the RMSEs of the model on the test dataset. And we further validate this criterion through evaluating the transferability of Model F on different systems at different temperatures by comparing the results given by DPMD and classical MD simulations.

Finally, it's worth saying that this study was unable to examine the impact of long-range interactions on the transferability of the DP models because such effects were completely neglected⁴⁵. It is conceivable that incorporating long-range interactions and other non-local effects could result in improvements in transferability. For example, the fourth-generation MLPs represent a promising approach^{44,72}. It is worth noting that these models require information on atomic charges, which was not available in our dataset. Considering the differences in transfer effects between Model S and Model F, our findings emphasize the influential role of building a strong training dataset in achieving a successful DP model. Especially the chemical environment of atoms should be adequately represented in training the DP model.

ASSOCIATED CONTENT

Supplemental Material

There are two parts in the Supplemental Material, computational details (S1 part) and supplemental figures or tables (S2 part). S1 part presents the construction of DP model, AIMD simulation details, DP-GEN scheme, descriptors and so on. S2 part offers supplemental figures (Figure S5-S14) to better illustrate the relevant content in the article. (PDF)

AUTHOR INFORMATION

Corresponding Author

Diannan Lu – Department of Chemical Engineering, Tsinghua University, Beijing 100084, P. R.

China; Email: ludiannan@tsinghua.edu.cn

Jianzhong Wu – Department of Chemical and Environmental Engineering, University of

California, Riverside, California 92521, United States; Email: jwu@engr.ucr.edu

Authors

Dongfei Liu – Department of Chemical Engineering, Tsinghua University, Beijing 100084, P. R.

China; Email: <u>ldf20@mails.tsinghua.edu.cn</u>

Author Contributions

The manuscript was written through contributions of all authors. All authors have given their

approval to the final version of the manuscript.

ACKNOWLEDGMENT

This work is supported and sponsored by the National Natural Science Foundation of China (No.

U1862204). The numerical calculations were performed at the "Tianhe-2" platform supported by

Guangzhou Supercomputer Centre.

27

REFERENCES

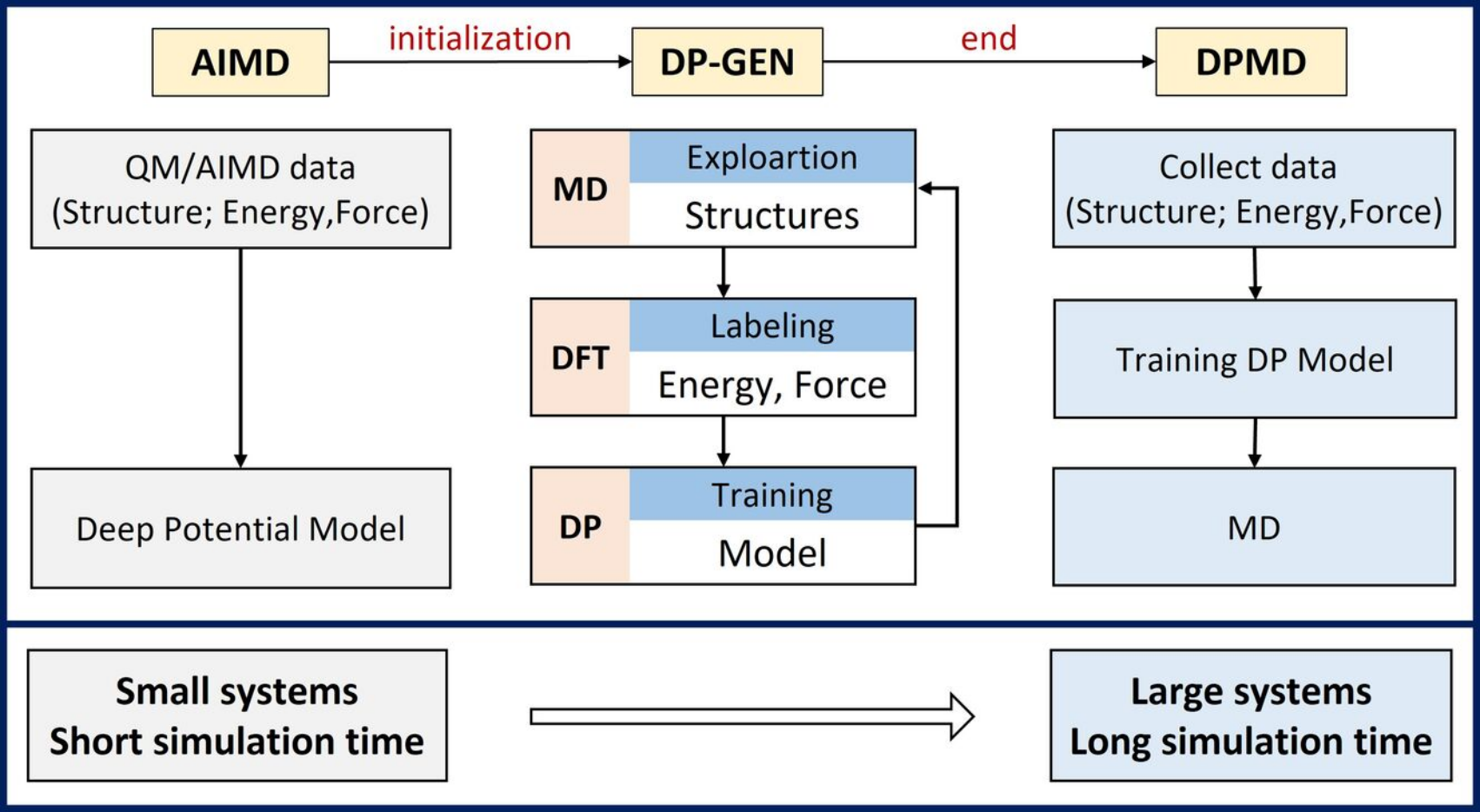
- (1) Whitby, M.; Quirke, N. Fluid Flow in Carbon Nanotubes and Nanopipes. *Nature Nanotech* **2007**, *2* (2), 87–94. https://doi.org/10.1038/nnano.2006.175.
- (2) Xie, Q.; Alibakhshi, M. A.; Jiao, S.; Xu, Z.; Hempel, M.; Kong, J.; Park, H. G.; Duan, C. Fast Water Transport in Graphene Nanofluidic Channels. *Nature Nanotech* **2018**, *13* (3), 238–245. https://doi.org/10.1038/s41565-017-0031-9.
- (3) Park, H. G.; Jung, Y. Carbon Nanofluidics of Rapid Water Transport for Energy Applications. *Chem. Soc. Rev.* **2014**, *43* (2), 565–576. https://doi.org/10.1039/C3CS60253B.
- (4) Chakraborty, S.; Kumar, H.; Dasgupta, C.; Maiti, P. K. Confined Water: Structure, Dynamics, and Thermodynamics. *Acc. Chem. Res.* **2017**, *50* (9), 2139–2146. https://doi.org/10.1021/acs.accounts.6b00617.
- (5) Kastelowitz, N.; Molinero, V. Ice–Liquid Oscillations in Nanoconfined Water. *ACS Nano* **2018**, *12* (8), 8234–8239. https://doi.org/10.1021/acsnano.8b03403.
- (6) Köhler, M. H.; Bordin, J. R.; de Matos, C. F.; Barbosa, M. C. Water in Nanotubes: The Surface Effect. *Chemical Engineering Science* **2019**, *203*, 54–67. https://doi.org/10.1016/j.ces.2019.03.062.
- (7) Wang, Q.; Liu, L.; Liu, C.; Song, J.; Gao, X. Size Effect in Determining the Water Diffusion Rate in Carbon Nanotubes. *Journal of Molecular Liquids* **2021**, *334*, 116034. https://doi.org/10.1016/j.molliq.2021.116034.
- (8) Falk, K.; Sedlmeier, F.; Joly, L.; Netz, R. R.; Bocquet, L. Molecular Origin of Fast Water Transport in Carbon Nanotube Membranes: Superlubricity versus Curvature Dependent Friction. *Nano Lett.* **2010**, *10* (10), 4067–4073. https://doi.org/10.1021/nl1021046.
- (9) Algara-Siller, G.; Lehtinen, O.; Wang, F. C.; Nair, R. R.; Kaiser, U.; Wu, H. A.; Geim, A. K.; Grigorieva, I. V. Square Ice in Graphene Nanocapillaries. *Nature* **2015**, *519* (7544), 443–445. https://doi.org/10.1038/nature14295.
- (10) Secchi, E.; Marbach, S.; Niguès, A.; Stein, D.; Siria, A.; Bocquet, L. Massive Radius-Dependent Flow Slippage in Carbon Nanotubes. *Nature* **2016**, *537* (7619), 210–213. https://doi.org/10.1038/nature19315.
- (11) Otake, K.; Otsubo, K.; Komatsu, T.; Dekura, S.; Taylor, J. M.; Ikeda, R.; Sugimoto, K.; Fujiwara, A.; Chou, C.-P.; Sakti, A. W.; Nishimura, Y.; Nakai, H.; Kitagawa, H. Confined Water-Mediated High Proton Conduction in Hydrophobic Channel of a Synthetic Nanotube. *Nat Commun* **2020**, *11* (1), 843. https://doi.org/10.1038/s41467-020-14627-z.
- (12) Liu, Y.-C.; Shen, J.-W.; Gubbins, K. E.; Moore, J. D.; Wu, T.; Wang, Q. Diffusion Dynamics of Water Controlled by Topology of Potential Energy Surface inside Carbon Nanotubes. *Phys. Rev. B* **2008**, *77* (12), 125438. https://doi.org/10.1103/PhysRevB.77.125438.
- (13) Muñoz-Santiburcio, D.; Marx, D. Nanoconfinement in Slit Pores Enhances Water Self-Dissociation. *Phys. Rev. Lett.* **2017**, *119* (5), 056002. https://doi.org/10.1103/PhysRevLett.119.056002.
- (14) Mallamace, F.; Broccio, M.; Corsaro, C.; Faraone, A.; Majolino, D.; Venuti, V.; Liu, L.; Mou, C.-Y.; Chen, S.-H. Evidence of the Existence of the Low-Density Liquid Phase in Supercooled, Confined Water. *Proceedings of the National Academy of Sciences* **2007**, *104* (2), 424–428. https://doi.org/10.1073/pnas.0607138104.
- (15) Cieplak, P.; Dupradeau, F.-Y.; Duan, Y.; Wang, J. Polarization Effects in Molecular Mechanical Force Fields. *J. Phys.: Condens. Matter* **2009**, *21* (33), 333102. https://doi.org/10.1088/0953-8984/21/33/333102.

- (16) Mendonça, B. H. S.; Ternes, P.; Salcedo, E.; de Oliveira, A. B.; Barbosa, M. C. Water Diffusion in Rough Carbon Nanotubes. *J. Chem. Phys.* **2020**, *152* (2), 024708. https://doi.org/10.1063/1.5129394.
- (17) Huang, L.-L.; Zhang, L.-Z.; Shao, Q.; Wang, J.; Lu, L.-H.; Lu, X.-H.; Jiang, S.-Y.; Shen, W.-F. Molecular Dynamics Simulation Study of the Structural Characteristics of Water Molecules Confined in Functionalized Carbon Nanotubes. *J. Phys. Chem. B* **2006**, *110* (51), 25761–25768. https://doi.org/10.1021/jp064676d.
- (18) Ho, T. A.; Striolo, A. Polarizability Effects in Molecular Dynamics Simulations of the Graphene-Water Interface. *The Journal of Chemical Physics* **2013**, *138* (5), 054117. https://doi.org/10.1063/1.4789583.
- (19) Mendonça, B. H. S.; Ternes, P.; Salcedo, E.; de Oliveira, A. B.; Barbosa, M. C. Water Diffusion in Carbon Nanotubes: Interplay between Confinement, Surface Deformation, and Temperature. *J. Chem. Phys.* **2020**, *153* (24), 244504. https://doi.org/10.1063/5.0031084.
- (20) Sam, A.; K, V. P.; Sathian, S. P. Water Flow in Carbon Nanotubes: The Role of Tube Chirality. *Phys. Chem. Chem. Phys.* **2019**, *21* (12), 6566–6573. https://doi.org/10.1039/C9CP00429G.
- (21) Cao, W.; Huang, L.; Ma, M.; Lu, L.; Lu, X. Water in Narrow Carbon Nanotubes: Roughness Promoted Diffusion Transition. *J. Phys. Chem. C* **2018**, *122* (33), 19124–19132. https://doi.org/10.1021/acs.jpcc.8b02929.
- (22) Li, S.; Schmidt, B. Replica Exchange MD Simulations of Two-Dimensional Water in Graphene Nanocapillaries: Rhombic versus Square Structures, Proton Ordering, and Phase Transitions. *Phys. Chem. Chem. Phys.* **2019**, *21* (32), 17640–17654. https://doi.org/10.1039/C9CP00849G.
- (23) Behler, J.; Parrinello, M. Generalized Neural-Network Representation of High-Dimensional Potential-Energy Surfaces. *Phys. Rev. Lett.* **2007**, *98* (14), 146401. https://doi.org/10.1103/PhysRevLett.98.146401.
- (24) Handley, C. M.; Popelier, P. L. A. Potential Energy Surfaces Fitted by Artificial Neural Networks. J. Phys. Chem. A 2010, 114 (10), 3371–3383. https://doi.org/10.1021/jp9105585.
- (25) Behler, J. Neural Network Potential-Energy Surfaces in Chemistry: A Tool for Large-Scale Simulations. *Phys. Chem. Chem. Phys.* **2011**, *13* (40), 17930. https://doi.org/10.1039/c1cp21668f.
- (26) Bartók, A. P.; Kondor, R.; Csányi, G. On Representing Chemical Environments. *Phys. Rev. B* **2013**, *87* (18), 184115. https://doi.org/10.1103/PhysRevB.87.184115.
- (27) Wang, H.; Zhang, L.; Han, J.; E, W. DeePMD-Kit: A Deep Learning Package for Many-Body Potential Energy Representation and Molecular Dynamics. *Computer Physics Communications* **2018**, 228, 178–184. https://doi.org/10.1016/j.cpc.2018.03.016.
- (28) Noé, F.; Tkatchenko, A.; Müller, K.-R.; Clementi, C. Machine Learning for Molecular Simulation. *Annual Review of Physical Chemistry* **2020**, *71* (1), 361–390. https://doi.org/10.1146/annurev-physchem-042018-052331.
- (29) Grisafi, A.; Nigam, J.; Ceriotti, M. Multi-Scale Approach for the Prediction of Atomic Scale Properties. *Chem. Sci.* **2021**, *12* (6), 2078–2090. https://doi.org/10.1039/D0SC04934D.
- (30) Huang, B.; von Lilienfeld, O. A. Ab Initio Machine Learning in Chemical Compound Space. *Chem. Rev.* **2021**, *121* (16), 10001–10036. https://doi.org/10.1021/acs.chemrev.0c01303.
- (31) Kocer, E.; Ko, T. W.; Behler, J. Neural Network Potentials: A Concise Overview of Methods. *Annual Review of Physical Chemistry* **2022**, *73* (1), 163–186. https://doi.org/10.1146/annurev-physchem-082720-034254.

- (32) Desai, S.; Reeve, S. T.; Belak, J. F. Implementing a Neural Network Interatomic Model with Performance Portability for Emerging Exascale Architectures. *Computer Physics Communications* **2022**, *270*, 108156. https://doi.org/10.1016/j.cpc.2021.108156.
- (33) Glick, Z. L.; Metcalf, D. P.; Koutsoukas, A.; Spronk, S. A.; Cheney, D. L.; Sherrill, C. D. AP-Net: An Atomic-Pairwise Neural Network for Smooth and Transferable Interaction Potentials. *J. Chem. Phys.* **2020**, *153* (4), 044112. https://doi.org/10.1063/5.0011521.
- (34) Smith, J. S.; Isayev, O.; Roitberg, A. E. ANI-1: An Extensible Neural Network Potential with DFT Accuracy at Force Field Computational Cost. *Chem. Sci.* **2017**, *8* (4), 3192–3203. https://doi.org/10.1039/C6SC05720A.
- (35) Lubbers, N.; Smith, J. S.; Barros, K. Hierarchical Modeling of Molecular Energies Using a Deep Neural Network. *J. Chem. Phys.* **2018**, *148* (24), 241715. https://doi.org/10.1063/1.5011181.
- (36) Zubatyuk, R.; Smith, J. S.; Leszczynski, J.; Isayev, O. Accurate and Transferable Multitask Prediction of Chemical Properties with an Atoms-in-Molecules Neural Network. *Science Advances* **2019**, *5* (8), eaav6490. https://doi.org/10.1126/sciadv.aav6490.
- (37) Unke, O. T.; Meuwly, M. PhysNet: A Neural Network for Predicting Energies, Forces, Dipole Moments, and Partial Charges. *J. Chem. Theory Comput.* **2019**, *15* (6), 3678–3693. https://doi.org/10.1021/acs.jctc.9b00181.
- (38) Chmiela, S.; Tkatchenko, A.; Sauceda, H. E.; Poltavsky, I.; Schütt, K. T.; Müller, K.-R. Machine Learning of Accurate Energy-Conserving Molecular Force Fields. *Science Advances* **2017**, *3* (5), e1603015. https://doi.org/10.1126/sciadv.1603015.
- (39) Bartók, A. P.; Payne, M. C.; Kondor, R.; Csányi, G. Gaussian Approximation Potentials: The Accuracy of Quantum Mechanics, without the Electrons. *Phys. Rev. Lett.* **2010**, *104* (13), 136403. https://doi.org/10.1103/PhysRevLett.104.136403.
- (40) Wood, M. A.; Thompson, A. P. Extending the Accuracy of the SNAP Interatomic Potential Form. *J. Chem. Phys.* **2018**, *148* (24), 241721. https://doi.org/10.1063/1.5017641.
- (41) Li, H.; Zhou, M.; Sebastian, J.; Wu, J.; Gu, M. Efficient Force Field and Energy Emulation through Partition of Permutationally Equivalent Atoms. *J. Chem. Phys.* **2022**, *156* (18), 184304. https://doi.org/10.1063/5.0088017.
- (42) Zhang, Y.; Wang, H.; Chen, W.; Zeng, J.; Zhang, L.; Wang, H.; E, W. DP-GEN: A Concurrent Learning Platform for the Generation of Reliable Deep Learning Based Potential Energy Models. *Computer Physics Communications* **2020**, *253*, 107206. https://doi.org/10.1016/j.cpc.2020.107206.
- (43) Schran, C.; Brezina, K.; Marsalek, O. Committee Neural Network Potentials Control Generalization Errors and Enable Active Learning. *J. Chem. Phys.* **2020**, *153* (10), 104105. https://doi.org/10.1063/5.0016004.
- (44) Behler, J. Four Generations of High-Dimensional Neural Network Potentials. *Chem. Rev.* **2021**, *121* (16), 10037–10072. https://doi.org/10.1021/acs.chemrev.0c00868.
- (45) Poltavsky, I.; Tkatchenko, A. Machine Learning Force Fields: Recent Advances and Remaining Challenges. *J. Phys. Chem. Lett.* **2021**, *12* (28), 6551–6564. https://doi.org/10.1021/acs.jpclett.1c01204.
- (46) Eckhoff, M.; Behler, J. From Molecular Fragments to the Bulk: Development of a Neural Network Potential for MOF-5. *J. Chem. Theory Comput.* **2019**, *15* (6), 3793–3809. https://doi.org/10.1021/acs.jctc.8b01288.
- (47) Eckhoff, M.; Schönewald, F.; Risch, M.; Volkert, C. A.; Blöchl, P. E.; Behler, J. Closing the Gap between Theory and Experiment for Lithium Manganese Oxide Spinels Using a High-

- Dimensional Neural Network Potential. *Phys. Rev. B* **2020**, *102* (17), 174102. https://doi.org/10.1103/PhysRevB.102.174102.
- (48) Zhang, L.; Wang, H.; Car, R.; E, W. Phase Diagram of a Deep Potential Water Model. *Phys. Rev. Lett.* **2021**, *126* (23), 236001. https://doi.org/10.1103/PhysRevLett.126.236001.
- (49) Gartner, T. E.; Zhang, L.; Piaggi, P. M.; Car, R.; Panagiotopoulos, A. Z.; Debenedetti, P. G. Signatures of a Liquid–Liquid Transition in an Ab Initio Deep Neural Network Model for Water. *Proc. Natl. Acad. Sci. U.S.A.* **2020**, *117* (42), 26040–26046. https://doi.org/10.1073/pnas.2015440117.
- (50) Yang, M.; Bonati, L.; Polino, D.; Parrinello, M. Using Metadynamics to Build Neural Network Potentials for Reactive Events: The Case of Urea Decomposition in Water. *Catalysis Today* **2022**, *387*, 143–149. https://doi.org/10.1016/j.cattod.2021.03.018.
- (51) Andrade, M. F. C.; Ko, H.-Y.; Zhang, L.; Car, R.; Selloni, A. Free Energy of Proton Transfer at the Water–TiO2 Interface from Ab Initio Deep Potential Molecular Dynamics. *Chem. Sci.* **2020**, *11* (9), 2335–2341. https://doi.org/10.1039/C9SC05116C.
- (52) Schran, C.; Thiemann, F. L.; Rowe, P.; Müller, E. A.; Marsalek, O.; Michaelides, A. Machine Learning Potentials for Complex Aqueous Systems Made Simple. *Proc. Natl. Acad. Sci. U.S.A.* **2021**, *118* (38), e2110077118. https://doi.org/10.1073/pnas.2110077118.
- (53) Wen, B.; Calegari Andrade, M. F.; Liu, L.-M.; Selloni, A. Water Dissociation at the Water–Rutile TiO2(110) Interface from Ab Initio-Based Deep Neural Network Simulations. *Proceedings of the National Academy of Sciences* **2023**, *120* (2), e2212250120. https://doi.org/10.1073/pnas.2212250120.
- (54) Quaranta, V.; Behler, J.; Hellström, M. Structure and Dynamics of the Liquid–Water/Zinc-Oxide Interface from Machine Learning Potential Simulations. *J. Phys. Chem. C* **2019**, *123* (2), 1293–1304. https://doi.org/10.1021/acs.jpcc.8b10781.
- (55) Quaranta, V.; Hellström, M.; Behler, J.; Kullgren, J.; Mitev, P. D.; Hermansson, K. Maximally Resolved Anharmonic OH Vibrational Spectrum of the Water/ZnO(101⁻0) Interface from a High-Dimensional Neural Network Potential. *The Journal of Chemical Physics* **2018**, *148* (24), 241720. https://doi.org/10.1063/1.5012980.
- (56) Artrith, N.; Kolpak, A. M. Understanding the Composition and Activity of Electrocatalytic Nanoalloys in Aqueous Solvents: A Combination of DFT and Accurate Neural Network Potentials. *Nano Lett.* **2014**, *14* (5), 2670–2676. https://doi.org/10.1021/nl5005674.
- (57) Kapil, V.; Schran, C.; Zen, A.; Chen, J.; Pickard, C. J.; Michaelides, A. The First-Principles Phase Diagram of Monolayer Nanoconfined Water. *Nature* **2022**, *609* (7927), 512–516. https://doi.org/10.1038/s41586-022-05036-x.
- (58) Thiemann, F. L.; Schran, C.; Rowe, P.; Müller, E. A.; Michaelides, A. Water Flow in Single-Wall Nanotubes: Oxygen Makes It Slip, Hydrogen Makes It Stick. *ACS Nano* **2022**, *16* (7), 10775–10782. https://doi.org/10.1021/acsnano.2c02784.
- (59) Zhang, L.; Lin, D.-Y.; Wang, H.; Car, R.; E, W. Active Learning of Uniformly Accurate Interatomic Potentials for Materials Simulation. *Phys. Rev. Materials* **2019**, *3* (2), 023804. https://doi.org/10.1103/PhysRevMaterials.3.023804.
- (60) Behler, J. Atom-Centered Symmetry Functions for Constructing High-Dimensional Neural Network Potentials. *The Journal of Chemical Physics* **2011**, *134* (7), 074106. https://doi.org/10.1063/1.3553717.
- (61) Kühne, T. D.; Iannuzzi, M.; Del Ben, M.; Rybkin, V. V.; Seewald, P.; Stein, F.; Laino, T.; Khaliullin, R. Z.; Schütt, O.; Schiffmann, F.; Golze, D.; Wilhelm, J.; Chulkov, S.; Bani-Hashemian, M. H.; Weber, V.; Borštnik, U.; Taillefumier, M.; Jakobovits, A. S.; Lazzaro,

- A.; Pabst, H.; Müller, T.; Schade, R.; Guidon, M.; Andermatt, S.; Holmberg, N.; Schenter, G. K.; Hehn, A.; Bussy, A.; Belleflamme, F.; Tabacchi, G.; Glöß, A.; Lass, M.; Bethune, I.; Mundy, C. J.; Plessl, C.; Watkins, M.; VandeVondele, J.; Krack, M.; Hutter, J. CP2K: An Electronic Structure and Molecular Dynamics Software Package Quickstep: Efficient and Accurate Electronic Structure Calculations. *J. Chem. Phys.* **2020**, *152* (19), 194103. https://doi.org/10.1063/5.0007045.
- (62) Liu, D.; Li, J.; Wu, J.; Lu, D. Ab Initio Molecular Dynamics Simulation of Water Transport through Short Carbon Nanotubes. *ACS Omega* **2022**, *7* (44), 40466–40479. https://doi.org/10.1021/acsomega.2c05588.
- (63) Jiang, W.; Zhang, Y.; Zhang, L.; Wang, H. Accurate Deep Potential Model for the Al-Cu-Mg Alloy in the Full Concentration Space*. *Chinese Phys. B* **2021**, *30* (5), 050706. https://doi.org/10.1088/1674-1056/abf134.
- (64) Zhang, L.; Han, J.; Wang, H.; Saidi, W. A.; Car, R.; E, W. End-to-End Symmetry Preserving Inter-Atomic Potential Energy Model for Finite and Extended Systems. arXiv December 20, 2018. http://arxiv.org/abs/1805.09003 (accessed 2022-10-29).
- (65) Zeng, J.; Zhang, L.; Wang, H.; Zhu, T. Exploring the Chemical Space of Linear Alkane Pyrolysis via Deep Potential GENerator. *Energy Fuels* **2021**, *35* (1), 762–769. https://doi.org/10.1021/acs.energyfuels.0c03211.
- (66) Rupp, M.; Tkatchenko, A.; Müller, K.-R.; von Lilienfeld, O. A. Fast and Accurate Modeling of Molecular Atomization Energies with Machine Learning. *Phys. Rev. Lett.* **2012**, *108* (5), 058301. https://doi.org/10.1103/PhysRevLett.108.058301.
- (67) Huo, H.; Rupp, M. Unified Representation of Molecules and Crystals for Machine Learning. *Mach. Learn.: Sci. Technol.* **2022**, *3* (4), 045017. https://doi.org/10.1088/2632-2153/aca005.
- (68) Goscinski, A.; Fraux, G.; Imbalzano, G.; Ceriotti, M. The Role of Feature Space in Atomistic Learning. *Mach. Learn.: Sci. Technol.* **2021**, *2* (2), 025028. https://doi.org/10.1088/2632-2153/abdaf7.
- (69) Langer, M. F.; Goeßmann, A.; Rupp, M. Representations of Molecules and Materials for Interpolation of Quantum-Mechanical Simulations via Machine Learning. *npj Comput Mater* **2022**, *8* (1), 41. https://doi.org/10.1038/s41524-022-00721-x.
- (70) Pronk, S.; Páll, S.; Schulz, R.; Larsson, P.; Bjelkmar, P.; Apostolov, R.; Shirts, M. R.; Smith, J. C.; Kasson, P. M.; van der Spoel, D.; Hess, B.; Lindahl, E. GROMACS 4.5: A High-Throughput and Highly Parallel Open Source Molecular Simulation Toolkit. *Bioinformatics* **2013**, *29* (7), 845–854. https://doi.org/10.1093/bioinformatics/btt055.
- (71) Jorgensen, W. L.; Chandrasekhar, J.; Madura, J. D.; Impey, R. W.; Klein, M. L. Comparison of Simple Potential Functions for Simulating Liquid Water. *The Journal of Chemical Physics* **1983**, 79 (2), 926–935. https://doi.org/10.1063/1.445869.
- (72) Ko, T. W.; Finkler, J. A.; Goedecker, S.; Behler, J. A Fourth-Generation High-Dimensional Neural Network Potential with Accurate Electrostatics Including Non-Local Charge Transfer. *Nat Commun* **2021**, *12* (1), 398. https://doi.org/10.1038/s41467-020-20427-2.



Original Systems System I System II **New Systems** System III System IV

